Microstructure-based discrete simulations of the compaction of refractory powder composites

Júlia Bonaldo, Stéphane Mazerat, Séverine Romero-Baivier, Christophe L Martin

Microstructure-based discrete simulations of the compaction of refractory powder composites

Julia C. Bonaldo[a,b], Stephane Mazerat[b], Severine Romero-Baivier[b], Christophe L. Martin[a,*]

[a] *Univ. Grenoble Alpes, CNRS, Grenoble INP, SIMaP, Grenoble, France*
[b] *Vesuvius group, 7011 Ghlin, Belgium*

Abstract

This work describes an original methodology to simulate the compaction behavior of carbon-bonded alumina refractories (Al_2O_3-C) by taking explicitly into account the microstructure of each composite phase. The Discrete Element Method (DEM) is used to model the composite as a mixture of fine and coarse alumina particles and graphite flakes. The binder phase, which typically represents 20% of the volume fraction, is accounted for by a specific contact law which adjusts the contact rigidity according to the indentation between the coated particles. Small indentations lead to a soft response while above a critical indentation, the contact becomes much stiffer when alumina particles are in direct contact. This simple model incorporates the granular behavior of the composite as well as the continuous matrix of the binder. matrix. Numerical composites with various compositions are numerically submitted to closed-die compaction. We show that the densification behavior during compaction depends primarily on the binder phase for the volume fractions studied here. The contribution of each phase (alumina, graphite, ...) to the total axial stress is investigated, thus providing new insights into the complex behaviour of these composites.

Keywords: discrete element method, powder compaction, refractory composites, Al_2O_3-C refractories, powder densification behavior, closed-die compaction

1. Introduction

Carbon-bonded alumina refractories (Al_2O_3-C) are heterogeneous and complex granular composites made of coarse alumina, graphite flakes, and a bonding matrix (mixture of fine

*Corresponding author
Email address: christophe.martin@grenoble-inp.fr (Christophe L. Martin)

alumina grains and binder). These composites are used for steel casting applications, e.g., for stoppers, ladle shrouds, or submerged nozzles. These refractory parts are designed to control the flow and velocity of the liquid steel and to prevent oxidation of the steel. The final refractory properties are governed both by the properties of the different composite phases and by the processing stages (mixing, compaction, and firing). Depending on the final shape of the industrial part, the powder composite may be compacted isostatically or uniaxially. The compaction may lead to density gradients along the part geometry resulting in thermo-mechanical properties mismatch. These mechanical property heterogeneities may induce stress concentrations, which, associated with extreme loading conditions, can lead to failure. Hence, understanding the link between the composite microstructure, its evolution during processing and the final thermo-mechanical properties is important for the development of new products and the improvement of the industrial process.

Because the powder compaction step is central to the forming of refractory composite materials, it is paramount to understand its effect on their microstructure evolution. In this context, compaction has been investigated in the literature both experimentally and numerically. Some experimental studies, for example, focused on investigating the densification behavior of a composite mixture composed of hard and soft particles during closed-die or isostatic compaction [1] [2] [3]. From a numerical point of view, the compaction stage has been studied mostly by the Finite Element Method (FEM) which treats the powder as a continuum and uses appropriate constitutive equations. The powder parameters applied in these equations need to be identified through a complex experimental characterization both for ceramic powders [4, 5], powders used for the pharmaceutical industry [6, 7], metal powders [8, 9], and refractory composites [10].

An alternative method to model the compaction behavior of powders is the Discrete Element Method (DEM), which explicitly considers the powder as a collection of discrete particles. The DEM may be used more effectively than FEM to clarify the link between the particulate microstructure and the behavior of the powder prior to and post-compaction. This approach of modeling the behavior of granular matter was pioneered by Cundall and Strack in 1979 [11] for geomaterials and has spread to engineering powder materials since then. Employing DEM [12, 13], or the multi-particle finite element method (MPFEM) [14,

15, 16, 17] on model powder materials, the compaction stage has been investigated. Some authors also studied the compaction behavior of model powder materials containing different particle sizes [18, 19] and particle size distributions [20]. In particular, the DEM has proved useful to understand the compaction of composite powders with soft (typically metallic) and hard (typically ceramic) particles mixed together [18].

This paper is mainly focused on the use of DEM simulations for modeling the compaction behavior of carbon-bonded alumina composites that are considered as model refractory materials, used in the steel casting process. These composites are made of hard (alumina and graphite) and soft (binder) phases and may be shaped via two routes: isostatic or closed-die compaction, depending on the final application.

The major part of the numerical and experimental studies concerning the powder compaction is related to composites made of metal-ceramic materials for the powder-metallurgy process. DEM simulations of the compaction of homogeneous refractory materials (alumina, magnesia) have been reported with various sizes of particles [20, 21]. However, as far as we know, no study has been reported yet in the literature regarding compaction simulations using DEM to model refractory composites on a mixture of hard particles and a soft binder. Especially, a direct link to the real microstructure is still missing in these works. The aim of this paper is to describe a methodology, based on DEM simulations, to account for the composite microstructure.

The present article is organized as follows. First, we present some essential information on the typical composite microstructure to be simulated. Second, the main characteristics of the DEM model, and in particular the contact laws are described. The composite in DEM is represented by a mixture of hard particle clusters (coarse alumina), single particles (fine alumina) and bonded particles (graphite). An original approach is presented to account for the binder as an elastic soft-shell covering alumina particles. The capability of this modeling approach to capture the densification behavior of complex refractory composites is highlighted by analysing the simulations at the scale of each phase. Experimental data on closed-die compaction are used throughout the paper for critical comparison with the simulation results.

2. Carbon-bonded alumina composites

A schematic representation of the composite refractory microstructure studied in this work is shown in Fig. 1 a). It can be thought of as an overlapping hierarchy, with a mesoscale made of coarse hard grains (white fused alumina with 250 µm average size) and graphite (<400 µm) reinforcing a matrix; itself constituted at microscale of fine grains (calcined alumina <50 µm) embedded into a pyrolytic carbonaceous binder (a mixture of resin and solvent).

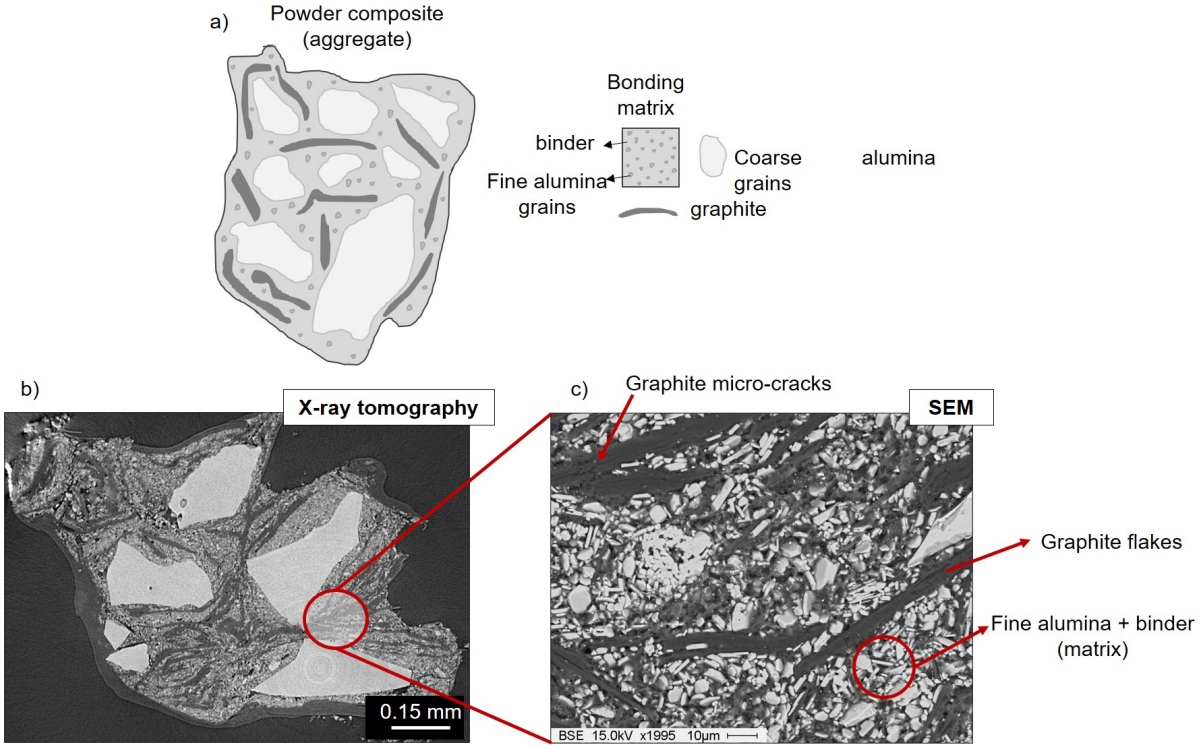

Figure 1: a) Schematic representation of a carbon-bonded alumina composite aggregate, composed of coarse grains and graphite flakes embedded into a continuum matrix. b) 2D slice from a 3D fragment image accessed through X-ray tomography analysis. c) Scanning electron microscope (SEM) image.

X-ray computed tomography analysis has been performed on the green mix aggregate sample to examine the overall microstructure arrangement after compaction (Fig. 1 b). The experiment consists of taking X-ray images of a sample tilted by a small angle for each image. The whole volume of the imaged specimen is re-constructed by assembling the digital images. The resulting 3D image is a superimposed projection of a volume in a 2D plane [22]. The observed aggregate has 1.2 mm size and the analysis was performed applying a resolution of 1.0 µm voxel size and 30 keV energy spectrum. Note that the gray levels in a CT slice

image correspond to the X-ray attenuation, i.e., reflecting the proportion of X-rays scattered or absorbed as they pass through each voxel. The X-ray attenuation is highly dependent on the X-ray energy, material density, and composition. Typically, alumina grains are denser and absorb more photons by the beam than porosity and graphite.

The geometry of coarse grains is dispersed in shape but generally angular, whereas the graphite flakes are mostly planar. The coarse alumina grains are visualized in different dimensions (average size of 250 µm). The graphite flakes exhibit some deformation due to the compaction stage. Three main phases could be distinguished: graphite, a bonding matrix (fine alumina and binder), and coarse alumina.

SEM (scanning electron microscope) analysis is also carried out on the final product (fired), displayed in Fig. 1 c). The image highlights mainly the matrix, appearing in grey at low magnification, which is composed of fine calcined alumina grains and a pyrolyzed binder. Fine alumina grains are also dispersed in shape, but some exhibit rounded shapes. Some graphite micro-cracks can be observed that are a consequence of the compaction and of the firing itself. However, the alumina grains remain unaffected.

Four model composites are investigated with different compositions (Table 1) to reflect the typical microstructure of industrial composites. Hereafter, the term matrix refers to the group (fine alumina + binder). Mix R is considered as the reference composite. The matrix of Mix 2 is characterized by a lack of binder (and excess of fine alumina grains). Mix 3 has an overall depleted matrix (40 % on Mix 3 against 45 % volume fraction on Mix R, Mix 2, and Mix 4) and an excess of coarse alumina grains and graphite. Mix 4, on the opposite exhibits a matrix with an excess of binder and lack of fine alumina grains. The objective in Mix 2 and Mix 3 is to generate a model composite with an excess of hard solid grains. In contrast, Mix 4 presents an excess of soft binder. Mix R can be considered as an intermediate to the other mixes.

3. Modeling particulate and continuous materials with DEM

An in-house DEM code dp3D, dedicated to engineering materials for modelling the compaction of refractory composites, is used. Spherical discrete elements are generated to model each phase of the composite with specific contact laws that describe the mechanical interac-

Refractory	Coarse alumina	Fine alumina	Graphite	Binder
Mix R (reference)	33	22.5	22	22.5
Mix 2	33	27.5	22	17.5
Mix 3	36	20	24	20
Mix 4	33	20	22	25

Table 1: Model refractory compositions in volume fraction %.

tions between them. As classically implemented in DEM, the spherical particles are displaced in the first half time-step according to the imposed increment in strain following the affine solution (homogeneous deformation of the sample). Contact forces are used to compute the total force acting on each particle. Newton's second law of motion enables the computation of the acceleration and an explicit time-integration scheme is used (velocity-Verlet) to obtain the new position of particles before a new affine strain increment is imposed. New contacts and lost contacts are updated at each time-step.

The graphite flakes and coarse alumina are represented as particle clusters (particle assemblies linked by elastic bonds). The fine alumina particles are modeled as single spheres with no bonds to represent a granular macroscopic behavior, characteristic of green materials (Fig. 2). The clusters (coarse alumina and graphite) are considered fully dense (relative density RD=1). This was attained simply by imposing an initial indentation between internal cluster particles such that the macroscopic relative density of the cluster is unity. This indentation is of the order of $0.29R$, where R is the sphere radius.

The graphite flakes present an elasto-plastic behavior, and may deform during compaction (particle bonds may deform and break, thus bringing some plasticity at the microscopic and macroscopic scales). The bonds in the coarse alumina clusters cannot fracture, contrary to the graphite. The bond interactions inside the coarse alumina particles are not calculated. In other words, spheres inside large alumina particles serve only to mesh them. Only spheres at the surface of these large alumina particles can interact mechanically with other particles. This type of cluster is generally referred as clump in the literature [23, 24].

The external and internal interaction contact models are summarized in Table 2 and schematically described in Fig. 3. The contact models (Hertzian and Bond) are described in

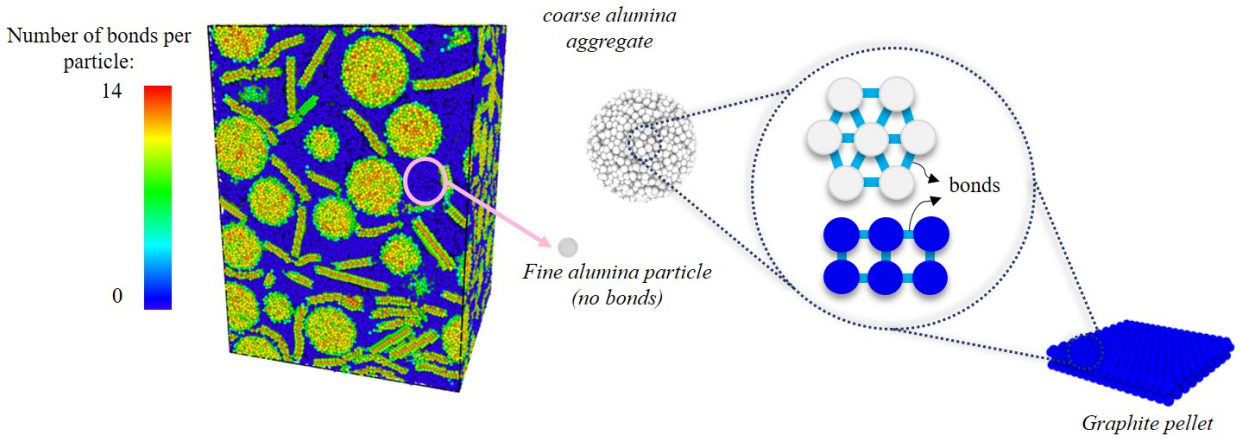

Figure 2: Typical discrete composite after compaction: from blue (no bonds) to red (with bonds). Coarse alumina and graphite are considered as an assembly of particles linked by bonds (cluster), and fine alumina as single non-bonded particles. Note how graphite flakes may deform while coarse alumina particles cannot.

the next section.

Composite phase	DEM model	External interactions	Internal interactions
Fine alumina	Single particle	Hertz (Eq. (1))	-
Coarse alumina	Particles cluster	Hertz (Eq. (1))	None
Graphite	Particles cluster	Hertz (Eq. (1))	Bond model (Eqs. (7), (8))

Table 2: Summary of the applied DEM model for each coarse alumina, fine alumina, and graphite phases (if single particle or particle cluster), and the external and internal interaction contact models.

3.1. Contact models

The Hertzian model is used to compute the normal force at the contact between two elastic particles, together with the Derjaguin Muller and Toporov (DMT) adhesion theory [25], which adds a tensile force to the standard repulsive Hertzian force. The normal force acting between two non-bonded particles with radii r_i and r_j, and elastic properties (E_i, ν_i) and (E_j, ν_j), respectively, is given by an Hertzian repulsive component (N^{Hertz}) and an adhesive tensile component (N^{DMT}) (compressive forces are considered as positive) [25, 26]:

$$N_e = N^{Hertz} + N^{DMT} = \frac{4}{3} E^* R^{*1/2} \delta_n^{3/2} - 2\pi\omega R^* \tag{1}$$

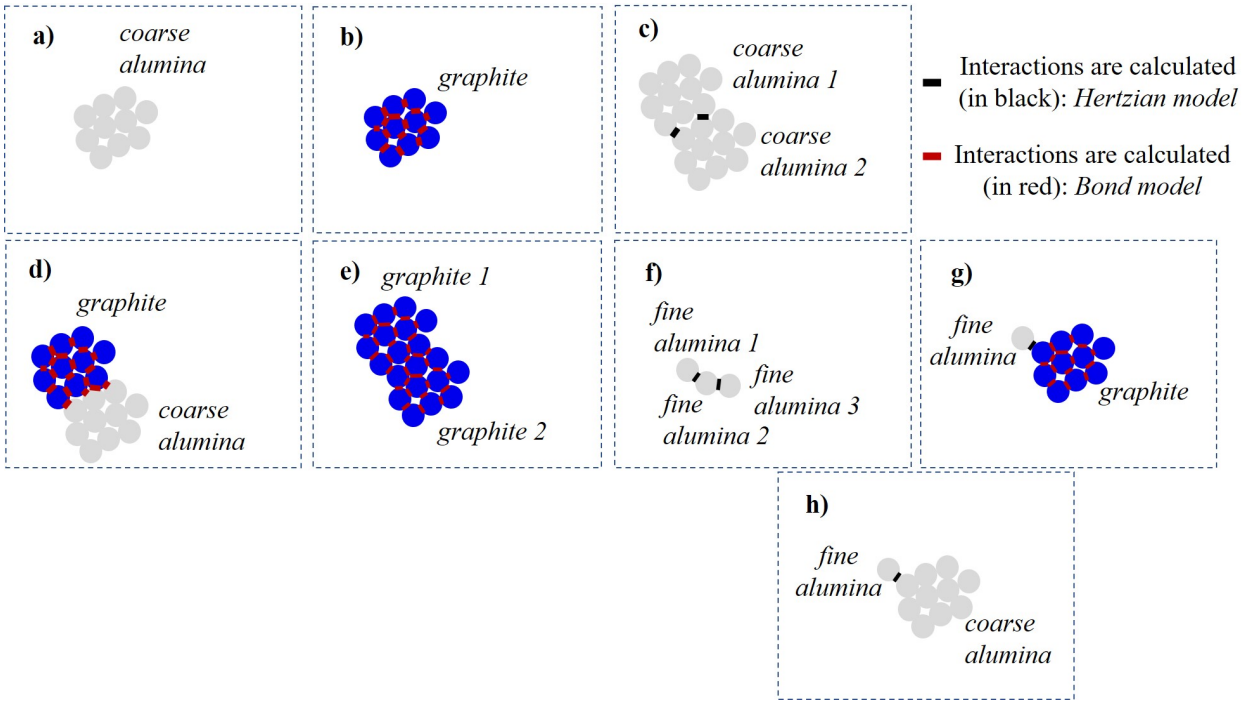

Figure 3: Schematic representation of the different type of contacts between the different discrete phases (fine alumina, coarse alumina and graphite).

where the effective Young's modulus between is:

$$E^* = \left(\frac{1-\nu_i^2}{E_i} + \frac{1-\nu_j^2}{E_j} \right)^{-1} \tag{2}$$

the equivalent radius R^* is:

$$R^* = \left(\frac{1}{r_i} + \frac{1}{r_j} \right)^{-1} \tag{3}$$

and where δ_n is the normal indentation, and $\omega = 2\gamma$ is the work of adhesion (with γ the surface energy). Decohesion occurs in the DMT model for a pull-off force $N^{DMT} = 2\pi\omega R^*$. The contact radius a is given by:

$$a^2 = R^* \delta_n \tag{4}$$

Contacts may also transmit frictional force (Hertz–Mindlin model) in the sticking mode while the tangential force is limited during sliding by Coulomb friction (friction coefficient μ). The friction law is implemented in incremental form at each time step $\mathrm{d}t$ by the friction force vector $\mathbf{T}$:

$$\mathrm{d}\mathbf{T} = -8G^* a \mathbf{v_t} \mathrm{d}t \qquad |\mathbf{T}| < \mu N^{Hertz} \tag{5}$$

$$\mathbf{T} \longleftarrow \frac{\mathbf{T}}{|\mathbf{T}|}\mu N^{Hertz} \qquad |\mathbf{T}| \geq \mu N^{Hertz} \tag{6}$$

where $\mathbf{v_t}$ is the tangential relative velocity at the contact and G^* is the equivalent shear modulus. Note that the condition for stick or slip ($|\mathbf{T}| < \mu N^{Hertz}$) applies on the repulsive part of the normal force (N^{Hertz}) and not on the total force N_e. In the slip condition, the vector $|\mathbf{T}|$ is capped by μN^{Hertz} but its direction is incrementally modified (Eq. (6)).

For bonded particles, the contact law is given by the analysis of [27] who studied the elastic response of bonded contact by the Finite Element Method (FEM). Two spherical particles (of the same material), connected to each other through a bond of radius a_b, transmit normal and tangential forces, and resisting moments. The normal contact force (N_b) for a bonded contact is given by:

$$N_b = \frac{2ER^*}{1-\nu^2} f_N(a^*, \Psi) a^* u_N \tag{7}$$

where E and ν are the Young's modulus and Poisson's ratio of the particles, $f_N(a^*, \Psi)$ is a function that depends on the relative radius of the bond ($a^* = \frac{a_b}{2R^*}$), Ψ is a geometric factor which allows for bond interaction to be considered, and u_N is the accumulated normal displacement at the contact [28]. The normal force can be either in compression ($u_N > 0$) or in tension ($u_N < 0$). The tangential contact force (T_b) is written as:

$$\mathbf{T_b} = \frac{4ER^*}{(2-\nu)(1+\nu)} f_T(a^*) a^* \mathbf{u_T} \tag{8}$$

where the function $f_T(a^*)$ depends on the relative bond size a^*, and, $\mathbf{u_T}$ is the accumulated tangential displacement vector at the contact. f_N and f_T values vary typically in between 1 and 2. More details concerning the form of $f_N(a^*, \Psi)$ and $f_T(a^*)$ used in this work can be found in earlier works [27, 28, 29, 30].

The maximum stress in tension (σ_N) and in shear (σ_T) can be evaluated by using the Potyondy's model [31]:

$$\sigma_N = \frac{N_b}{\pi {a_b}^2} - 4\frac{|M_T|}{\pi {a_b}^3} \tag{9}$$

$$\sigma_T = \frac{T_b}{\pi {a_b}^2} + 2\frac{|M_N|}{\pi {a_b}^3} \tag{10}$$

where M_N and M_T are the bonds resisting moments in the normal and tangential directions,

respectively:

$$M_N = -\frac{8ER^{*3}}{(2-\nu)(1+\nu)} f_T(a^*)\theta^N \tag{11}$$

$$M_T = -\frac{2ER^{*3}}{(1-\nu^2)} f_N(a^*, \Psi)\theta^T \tag{12}$$

where θ^N and θ^T are the accumulated relative rotations in the normal and tangential directions, respectively.

Regarding the failure criteria applied in our work at a bonded contact, Eqs. (9) and (10) give at each time step an evaluation of the stress in tension and shear acting on the bond. If one of these stresses is above the tension strength (Σ_N) or shear strength (Σ_T), the bond is considered as broken. A fractured bond may transmit a shear force according to a Hertz-Mindlin friction law (Eq. (6)). Correspondingly, a fractured bond in shear continues to transmit a resisting moment in the tangential direction but none in the normal direction.

3.2. Binder shell model

The contact laws described above are classic laws for elastic and bonded interactions. The very soft binder phase that coats hard particles (fine alumina particles or coarse alumina particles) introduces a different issue. We simply take the binder into account by stating that the stiffness of a contact depends on the mutual indentation of particles. For a small enough indentation, the contact stiffness is dictated by the binder (soft phase) whereas for an indentation larger than a critical value (linked to the binder thickness on the particles), the stiffness is dictated by the hard alumina (hard phase). Note that we have observed that graphite flakes are more difficult to be coated properly with binder. Thus, the binder model applies only to fine and coarse alumina particles. Still, contacts between an alumina particle and a graphite flake are affected by the binder but with a smaller thickness.

Consider two hard particles with Young's moduli (E_i, E_j) coated by a binder shell with thickness t_i and t_j. The total radii of the particles (with the binder) are r_i and r_j. We note E_{binder}, the Young's modulus of the binder. In this model, the effective Young's modulus (Eq. (2)) used in Eq. (1) is simply multiplied by a factor $\frac{E_{alumina}}{E_{binder}}$ when entering the hard phase branch. The transition from the soft phase to the hard phase depends on the mutual indentation and on the thickness of the binder.

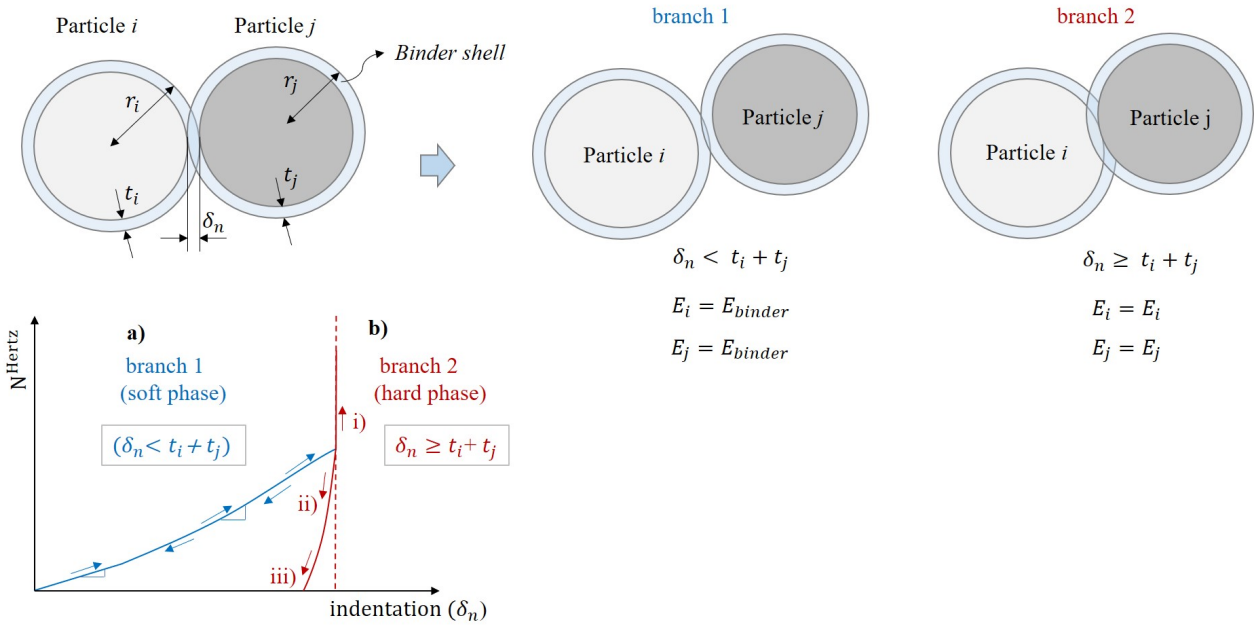

Figure 4: Schematic representation of a contact between two hard particles coated with a binder of thickness t_i and t_j. a) the contact remains within the soft elastic binder phase (branch 1). b) when the indentation reached a critical value i.e., condition $\delta_n \geq t_i + t_j$ applies, the elastic modulus of particles i and j are multiplied by a factor α and the contact enters branch 2. Once in branch 2, the contact may i) continue to load in compression, ii) unload, or iii) fail (if $\delta_n \leq (t_i + t_j)\left(1 - \frac{1}{\alpha}\right)^{\frac{2}{3}}$).

Fig. 4 graphically summarizes the binder model in the case of two coated particles (fine or coarse alumina). In branch 1 (soft phase) and in the general case of two coated (alumina) or non-coated (graphite) particles:

$$N^{Hertz} = \frac{4}{3}\left(\frac{1-\nu_i^2}{\alpha_i E_i} + \frac{1-\nu_j^2}{\alpha_j E_j}\right)^{-1} R^{*1/2}\delta_n^{3/2} \qquad 0 < \delta_n \leq t_i + t_j \tag{13}$$

with $\alpha = \frac{E_{binder}}{E_{alumina}}$ for alumina and $\alpha = 1$ for graphite. If the contact has not entered previously branch 2 (hard phase), any unloading in branch 1 is fully reversible. If the indentation reaches the critical indentation $t_i + t_j$:

$$N^{Hertz} = \frac{4}{3}\left(\frac{1-\nu_i^2}{E_i} + \frac{1-\nu_j^2}{E_j}\right)^{-1} R^{*1/2}\delta_n^{3/2} \qquad \delta_n > t_i + t_j \tag{14}$$

Two coated alumina particles interact directly through the hard alumina phase in branch 2. Note that in our case the hard phase stiffness is much larger than the binder's stiffness. Thus, the indention increase is very small in branch 2.

If the contact unloads from branch 2, (Fig. 4 ii), the elastic properties in eq. (14) are kept constant. This is to mimic the extrusion of the binder at the contact between the two hard particles. The contact may fail (Fig. 4 iii) if the condition: $\delta_n \leq (t_i + t_j)\left(1 - \frac{1}{\alpha}\right)^{\frac{2}{3}}$ applies. In that case no normal force is transmitted at the contact.

Hysteresis is introduced in the model since a contact that has entered branch 2 will not unload reversibly through branch 1. It should be clear that this model is a very simplistic idealization of the complex behaviour of hard particles coated with a soft binder. In particular, the binder plasticity (or viscoplasticity) is oversimplified. Still, our model allows for a simple representation of particles that behave with a small stiffness when slightly indented (beginning of the compaction) and exhibit a much larger stiffness when indented above a critical value (end of the compaction).

As stated above, the binder model applies only to fine and coarse alumina particles. For contacts between alumina particles and graphite flakes, the total binder thickness $(t_i + t_j)$ in Eqs. (13) and (14) is solely given by the alumina binder thickness. Thus, contacts between alumina and graphite particles are affected by the binder, but with a lesser thickness, which models very crudely the poorer coating of the graphite flakes.

3.3. Binder thickness calculation

The binder shell thickness of each composite (Mix R to 4) can be related to its composition, calculated from the volume fraction of each component (coarse and fine alumina, graphite, and binder). We use subscripts ca, fa and g for *coarse alumina*, *fine alumina*, and *graphite*, respectively.

Note that all spherical discrete elements have the same diameter (7.8 µm), which corresponds to the mean size of the fine alumina particles. This allows for more efficient CPU processing of contact detection in the DEM code. The coarse alumina cluster (made approximately of 4,600 spherical particles) is about 135 µm in size. For simplicity, it is approximated to be a sphere-like cluster. The graphite flake (made of 1,070 spherical particles) is represented by a parallelepiped with dimensions of 121 µm × 116 µm × 17 µm.

The binder volume fraction $V_{f(binder)}$ is:

$$V_{f(binder)} = (V_{binder(ca)} + V_{binder(fa)})/(V_{ca} + V_{fa} + V_g) \tag{15}$$

where $V_{binder(ca)}$, $V_{binder(fa)}$ are the total binder volumes surrounding the coarse alumina clusters and fine alumina particles, and V_{ca}, V_{fa}, and V_g are the coarse, fine alumina, and, graphite volumes, respectively. We assume that the binder thickness on coarse alumina and fine alumina particles is the same, and hereafter noted t. $V_{binder(ca)}$ and $V_{binder(fa)}$ can be simply computed from the number of coarse and fine alumina particles introduced in the simulation (n_{ca}, n_{fa}) and their radii (r_{ca}, r_{fa}):

$$V_{binder(ca)} = n_{ca}\frac{4}{3}\pi(r_{ca}^3 - (r_{ca} - t)^3) \tag{16}$$

$$V_{binder(fa)} = n_{fa}\frac{4}{3}\pi(r_{fa}^3 - (r_{fa} - t)^3) \tag{17}$$

Table 3 lists the typical numbers of discrete elements and particles introduced in simulations once the number of coarse alumina clusters is fixed for each mix. The total number of discrete elements is characteristic of the Representative Volume Element chosen for our simulations (see section 5).

Mix	phase	binder thickness (μm)	number of particles	total number of discrete elements
Mix R	Coarse alumina	0.774	8	117,605
	Fine alumina	0.774	53,695	
	Graphite	-	25	
Mix 2	Coarse alumina	0.569	8	118,499
	Fine alumina	0.569	54,589	
	Graphite	-	25	
Mix 3	Coarse alumina	0.893	8	117,109
	Fine alumina	0.893	53,199	
	Graphite	-	25	
Mix 4	Coarse alumina	0.771	10	132,812
	Fine alumina	0.771	53,192	
	Graphite	-	31	

Table 3: DEM main parameters for each composition.

3.4. Macroscopic stress calculation

The macroscopic stress tensor at the scale of the entire packing is computed by using the total contact force at each contact (normal and tangential components) and the branch vector connecting the centers of the two particles p and q in contact ($\mathbf{l}_{p,q}$). The macroscopic stress tensor is calculated from Love's formulation [32] [33]:

$$\sigma_{ij} = \frac{1}{V} \sum_{contacts} (N_i + T_i) l_{pq,j} \tag{18}$$

where the summation is carried out on all contacts transmitting forces in the packing and where V is the sample volume, N_i and T_i are the i^{th} components of the normal and tangential contact forces at the contact, respectively. $l_{pq,j}$ is the j^{th} component of the $\mathbf{l}_{pq}$ branch vector.

When modeling a composite made of a mixture of distinct phases, it is also useful to calculate the macroscopic stress contribution of each phase separately. Thus, similarly to Eq. (18), the stress tensor associated to phase P is defined as:

$$\sigma_{ij,P} = \frac{1}{V} \sum_{contacts,P} (N_i + T_i)(r - \frac{1}{2}\delta_n) n_j \tag{19}$$

where n_j is the j^{th} component of the contact normal vector $\mathbf{n}$. And, r is the radius of the discrete element of phase P for a given contact. Note that in Eq. (19), the sum is made on all contacts that include a particle of phase P. The total macroscopic stress tensor (Eq. (18)) is retrieved by summing all contributions from each phase P from Eq. (19). This is because the branch vector in Eq. (18) is replaced here by the term $(r - \frac{1}{2}\delta_n)\mathbf{n}$.

4. Generation of numerical microstructures and compaction simulations

Fig. 5 depicts the three stages that are used to characterize a mix from its generation (Fig. 5 a) to the compaction (Fig. 5 c). The initial composite assembly is obtained by first randomly locating bonded particle clusters (graphite and coarse alumina) and non-bonded single particles (fine alumina) in a parallelepipedic periodic cell with (1x1x2) size ratio (Fig. 5 a). At this stage (denominated gas of particles), there is no contact between constituents (fine alumina, coarse alumina, and graphite flakes) and the relative density is small (0.4). The number of discrete elements for each phase is chosen to obtain the correct composition for a given mix (see table 3). Note that by modifying the random seed used to produce a given

initial gas of particles, we can produce several packings that exhibit the same macroscopic properties (essentially the same composition), but with particles located differently. This is useful to evaluate dispersion in our simulations. We have used 5 different random seeds for each condition to generate error bars.

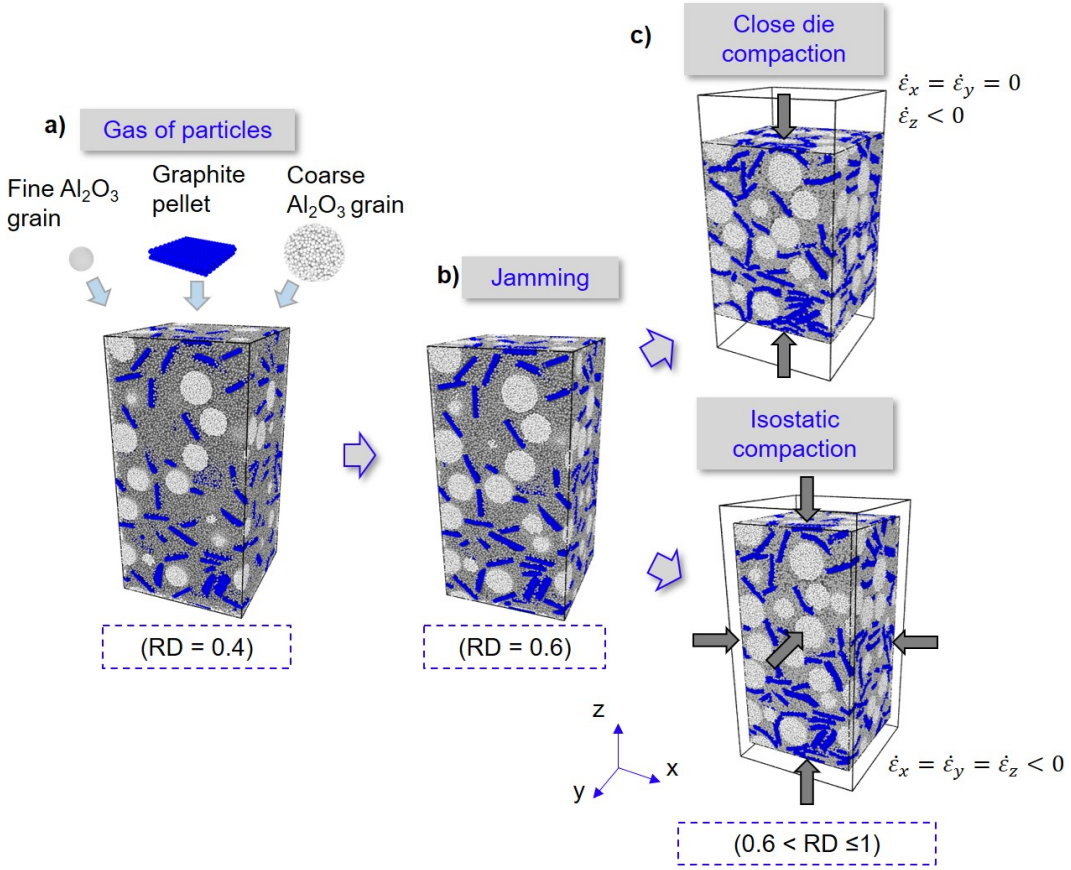

Figure 5: DEM simulations steps performed in this work: a) Particles/aggregates are randomly located inside a box with periodic conditions up to a density RD = 0.4. b) the packing is densified until RD = 0.6. c) close-die or isostatic compaction simulations are used to investigate the minimum RVE size (section 5).

This initial microstructure is further jammed by isostatic densification under a small macroscopic pressure (0.02 MPa) up to a relative density of 0.6 (Fig. 5 b) [34, 35]. During this jamming stage, only elastic interactions are considered (Eq. (1)). Friction and adhesion between particles are set to zero. The jamming stage mimics the gentle rearrangement of particles in the die without any plasticity or bond breakage. The jammed numerical packing at RD=0.6 represents the mix in the die before compaction. This value of the RD before compaction has been chosen to be in agreement with experimental observations.

From the jammed state, the numerical microstructure can be compacted along two routes: closed-die or isostatic compaction (Fig. 5 c). In close-die compaction, the packing is compacted by imposing an axial strain-rate ($\dot{\varepsilon_z}$) in the z direction and a null strain-rate on x and y axis. Although we do not simulate the die itself, these conditions (uniaxial compaction) should simulate correctly the typical stress conditions encountered by a composite powder during close-die compaction (far from the die). In isostatic compaction, an identical compressive strain-rate is imposed on all three axis.

The imposed strain-rates are adjusted during simulations to ensure quasi-static conditions (force equilibrium). The normalized kinetic energy per particle [36] is used as the criterion for adjusting strain-rates:

$$\tilde{E}_{kin} = \frac{E_{kin}}{n \max(Nr)} \leq 10^{-7} \tag{20}$$

where E_{kin} is the total kinetic energy of the particle system, n the total number of particles, and $\max(Nr)$ is the maximum value for all contacts of the product of the normal force N and discrete element radius r.

5. Representative volume element

Figs. 2 and 5 show the typical simulation box with fine alumina, coarse alumina and graphite flakes to form a composite. In these figures, the total number of particles is approximately 600k. Because the microstructure is quite complex with large size ratio between the fine alumina and coarse alumina particle, a three-dimensional Representative Volume Element (RVE) must be found to ensure that the results do not depend on the particle number while minimizing the CPU time. We use two criteria to determine the RVE: convergence of the macroscopic stress (at RD=0.95) and isotropy. The macroscopic response of the composite should be isotropic (due to the random orientation of the graphite flakes). We tested this through isostatic compaction simulations performed on RVEs containing increasing number of discrete elements. All RVEs are generated with the composition of mix R (reference composite).

For each RVE, five different packings were generated using five different random seeds to locate the particles initially in the simulation box. A total of 30 RVEs are used from isostatic

compaction simulations to allow deviation measurement. The mean (Σ_m) and deviatoric (Σ_d) stresses are calculated and plotted in Fig. 6.

Fig. 6 shows that too small RVEs with $n \approx 14000$ discrete elements exhibit a large deviation, a non-isotropic behavior and a too large mean stress as compared to larger RVEs. For an RVE with $n \geq 380,000$ discrete elements, stresses converge with a much lower standard deviation. Larger RVEs confirm this trend with a clear convergence of both Σ_m and Σ_d. Fig. 6 shows that an RVE with $n \geq 117,605$ discrete elements is large enough to ensure a good convergence of Σ_m and Σ_d with reasonable standard deviation.

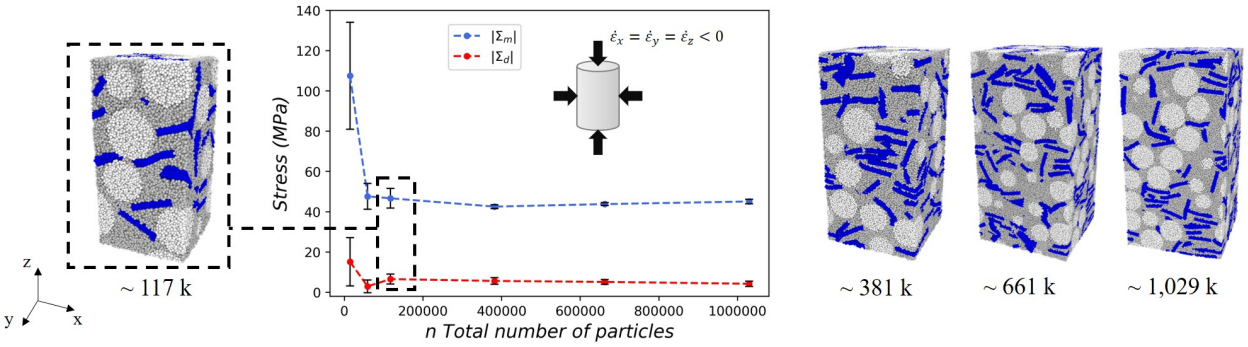

Figure 6: Evolution of the macroscopic deviatoric (Σ_d) and mean (Σ_m) stresses, in module, against the total number of particles, at the end of isostatic compaction simulations (density RD = 0.95).

We have repeated the isostatic compaction RVE study for closed-die compaction conditions and observed a similar behavior. In other words, a total number of particles n of the order of 110, 000 is sufficiently large to ensure a good convergence and reasonable CPU time on both isostatic and closed-die compaction configurations. The typical total clock time using 8 CPUs (openMP parallelization) is 25 hours for $n = 117,605$ discrete elements and is approximately linear with n. All results shown hereafter are obtained with n of the order of 100, 000 particles (depending on the exact composition of the mix).

6. Closed-die compaction simulations

The closed-die compaction of the four mixes described in section 2 has been simulated. These simulations are compared with experimental data obtained from single-action pressing in a steel die for a maximum axial stress of 35 MPa. Experimental relative density was measured by recording the piston displacement. The finite rigidity of the set-up was measured by

running piston to piston pressing (no powder), and the related displacement was subtracted to the piston displacement to obtain the correct relative density (RD).

6.1. Phase properties

The material parameters at the microscopic scale that enter contact laws (Eqs. (1), (5-12) have been determined to retrieve the macroscopic properties (elasticity and fracture) of alumina and graphite phases. The identification methodology has been described in details elsewhere for elasticity [35] and fracture [37]. Concerning the binder, the value of the elastic modulus has been calibrated using the macroscopic compaction curve of mix R (reference mix). This value (approximately 1 GPa) is much lower than for alumina and graphite phases, as it should for a pyrolytic carbonaceous binder.

The material parameters chosen for the simulations are listed in Table 4. Note that the Poisson's ratio has almost no effect and has been chosen as 0.2 for all materials for simplicity. The friction coefficient has also been set to a reasonable value of 0.2 for all contacts. We have observed that its effect is also of second order on the axial macroscopic stress during closed-die compaction.

Binder stiffness is the material parameter that most affects the macroscopic compaction behaviour of refractory composites. Fig. 7 shows simulations for increasing E_{binder} from 0.1 to 3 GPa for mix R (with E_{binder} = 1.0GPa, the value chosen for standard simulations). The simulation curves are typical of closed-die compaction with an initial flat curve that is characteristic of particle rearrangement followed by an increase of the axial stress when the various phases in the mix deform at the contact (binder coated particles, graphite flakes). The last stage of the compaction is an asymptotic increase of the stress when large RDs are attained. Fig. 7 shows that the relative density attained at the maximum axial stress (35 MPa) decreases markedly as the binder rigidity increases. This indicates the importance of the binder phase (with approximately 20% volume fraction of binder) in such composites. The objective of the following sections is to better understand, using the wealth of information provided by DEM simulations, the role of the binder and its interaction with other phases.

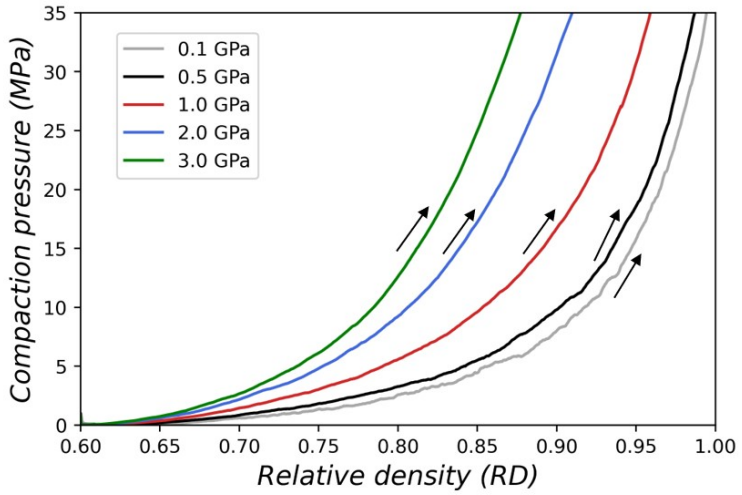

Figure 7: Evolution of the axial stress during closed-die compaction of Mix R with various values of E_{binder}.

Phase	γ (J/m^2)	μ	$\sigma_N = \sigma_T$ (MPa)	E (GPa)	ν
Coarse alumina	28	0.2	-	380	0.2
Fine alumina	28	0.2	-	380	0.2
Graphite	28	0.2	150	35	0.2
Binder	-	0.2	-	1.0	0.2

Table 4: Material parameters of contact laws used for compaction simulations for the four phase of the mixes.

6.2. Composites densification behavior

Eq. (19) allows to evaluate the contribution of each phase of the mix on the total macroscopic stress. The evolution of the axial stresses associated with each phase (fine coated alumina, coarse coated alumina, and graphite) and the total macroscopic axial stress against the relative density are shown in Fig. 8 for mix R. The binder phase contribution is not explicitly included here as it is gathered together with fine coated alumina and coarse coated alumina. Fig. 8 also shows the experimental data with a good agreement with DEM. This validates the calibration of the binder stiffness. Note in particular that the curve shape is well rendered by the DEM simulation.

Fig. 8 allows sorting the contribution of each phase. Recall that a contact between two different phases (for example coarse alumina and fine alumina) is accounted in the contribution of the two phases (with a 1/2 factor approximately since the branch vector in Eq. (18)

is replaced by the term $(r - \frac{1}{2}\delta_n)\mathbf{n}$). Fig. 8 indicates that the fine coated alumina particles and the graphite flakes have the most important contributions and that the coarse alumina coated particles have only a minor effect on the total stress. This result is not intuitive in a continuum mechanics framework since all phases have similar volume fractions and coarse alumina is the dominant phase in volume fraction (33%). It should be understood by recalling that the material to be compacted is a particulate material with particles interacting through their contacts. Because coarse alumina particles are large in size, they generate only a few contacts that do not percolate. The more numerous contacts between fine alumina particles have a much greater impact.

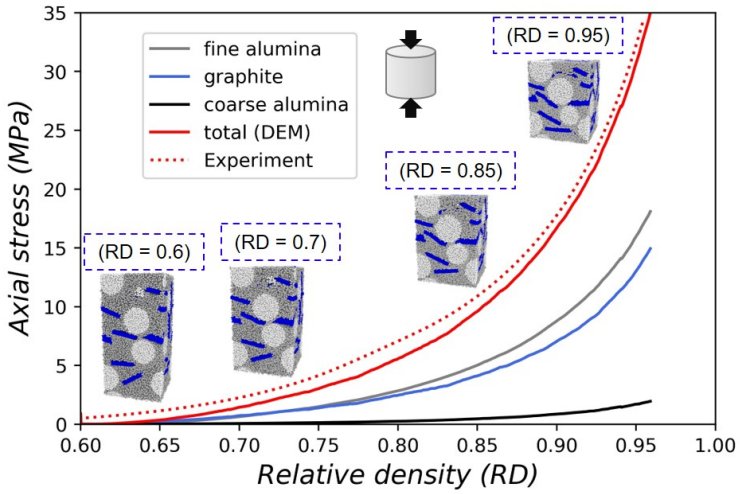

Figure 8: DEM close-die compaction: contribution of the three different discrete phases (fine alumina, coarse alumina, and graphite) to the axial macroscopic stress (final target: σ_z=35 MPa). Comparison of the total stresses evolution during a DEM closed-die compaction simulation and experiment (Mix R).

The above result for mix R, is confirmed for the four mixes by examining the contribution of each phase. This is carried out in Fig. 9, which gives the axial stress contributions attained for a target density RD=0.90 for all four mixes. Again, the dominant effect of fine alumina and graphite phases on the total macroscopic stress is clear for the four mixes. Fig. 9 demonstrates that the binder volume fraction (accounted for in the DEM simulations by varying the binder layer thickness (see section 3.2)) is the best predictor for the ranking of the four mixes in terms of their ability to densify. This ranking is in good accordance with experimental data for the four mixes. Note that DEM material parameters are the same

for all four mixes, while the mix composition is solely accounted for by varying the particle numbers and the binder thickness.

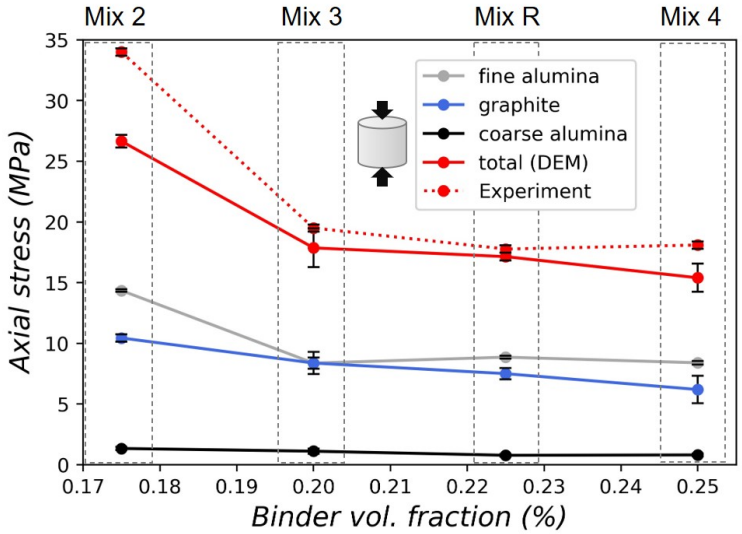

Figure 9: Contribution of the macroscopic axial stress related to each discrete phase (coarse alumina, graphite, and fine alumina) to the total macroscopic axial stress (σ_z) of composites (Mix R to 4), against the binder volume fraction (in %), during close-die compaction simulations (target: density RD=0.90). Comparison with experimental data obtained for the four mixes.

6.3. Contact behaviour of coated particles

Figs. 8 and 9 give valuable information on the contributions of the hard phases (alumina and graphite) during compaction. However, they still conflate the effect of the binder with those phases. To better understand the effect of the binder on the composite densification during closed-die compaction, it is necessary to analyze the behavior at the particle contact length scale.

For this purpose, the interactions between coated or non-coated particles has been recorded all along closed-die compaction for Mix R (reference composite) with a target of 35 MPa for the axial stress. Four typical contacts have been tagged and their normal contact force evolution was examined. The four contacts are coarse alumina - graphite (1), fine alumina - graphite (2), coarse alumina - fine alumina (3), and fine alumina - fine alumina (4). The evolution of a contact between two coarse alumina particles is not presented as this type of contact is very rare.

The evolution of the normal contact force (N^{Hertz}) (Eq. (1)), against the particle indentation normalized by the particle radius r, $\tilde{\delta_n} = \delta_n/r$, is shown in Figs. 10 a1) and a2). Note that the initial normal force is negative (tensile force) as adhesion is introduced only in the compaction simulation (the jamming stage is conducted with neither friction nor adhesion). Figs. 10 a1) and a2) illustrate the stiff transition from a binder dominated contact to a hard phase dominated one, with the material parameters from table 4. The critical value at which this transition occurs depends on the total binder thickness that coats the two particles (t_i+t_j in Eqs. (13) and (13)). Since we assume that graphite flakes are poorly coated ($t_2 = 0$), the transition for contacts involving graphite occurs at approximately half that for contacts with only alumina particles (≈ 0.2 and 0.4, respectively).

When the transition is reached, the relative indentation $\tilde{\delta_n}$ does not increase anymore (although the hard phase stiffness is finite) and the contact loads and unloads in the hard-phase branch. Contact (1) between a coarse alumina particle and a graphite flake exemplifies such a behaviour. Figs. 10b shows the history of the four contacts as relative density increases from 0.6 to 0.97. Contact (1) reaches the critical indentation (marked by a star) soon in the compaction and stays in the hard phase branch afterward. The contact is lost at approximately 0.87 RD but the memory of its transition to branch 2 is kept in the simulation and further reloading when the contact is resumed is characteristic of branch 2.

Contact (2) exhibits a similar behaviour to contact (1) but is never lost during compaction. Contact (3) shows the typical behaviour of a contact between two hard particles. The transition occurs at a rather large value of $\tilde{\delta_n}$ (≈ 0.4) as the two particles are coated with binder. Contact (4) illustrates the fact that some contacts never reach branch 2 and keep a soft behaviour all along the compaction.

These four examples represent only a fraction of the hundreds of thousands of contacts that arise in the simulation. Fig. 11 allows for a more quantitative understanding of how contacts evolve from the soft to the hard branch. It shows the fraction of contacts in a given branch for the five types of contact that have non-negligible contributions to the total macroscopic stress.

Below RD=0.85, the fraction of contacts between fine alumina particles corresponds to approximately 80% of interactions in the soft binder (Fig. 11 a)) . Above RD=0.85, a gradual

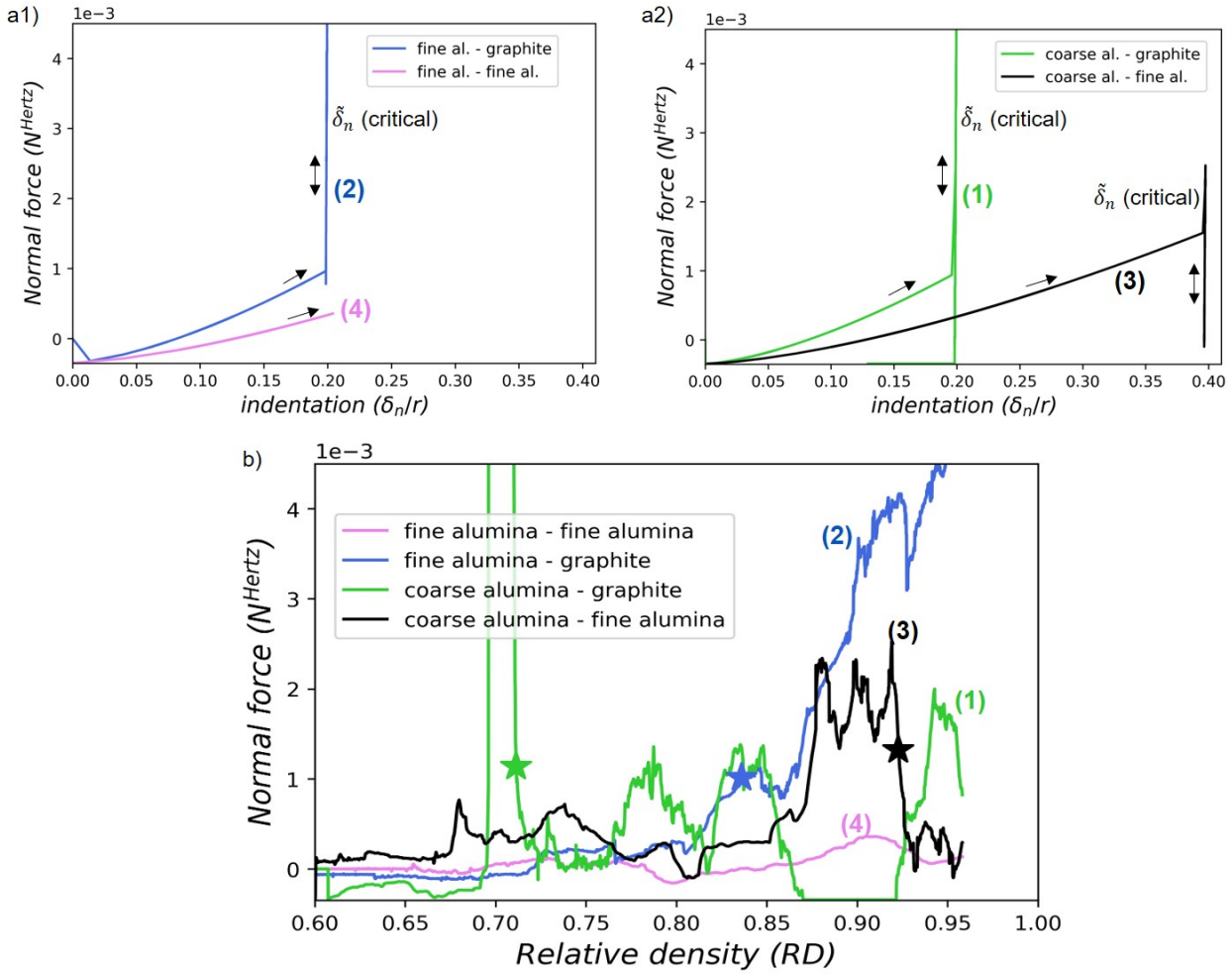

Figure 10: DEM close-die compaction simulation (target σ_z=35 MPa, Mix R). a1) and a2) Normal Hertzian contact force evolution (N^{Hertz}) versus normalized particle indentation (δ_n/r). Contacts type 1) to 4) represent the particle contact between three components (coarse alumina, fine alumina, and graphite). Once the contact reaches the critical indentation value ($\tilde{\delta_n}$), hard contacts appear. b) N^{Hertz} versus composite relative density (RD). $*$ represents the point where the interactions move towards the hard branch.

decrease is observed, associated with an increase of the fraction of direct contacts between alumina particles (Fig. 11 b)). This increase explains in part the asymptotic behaviour of the axial stress at large densities (Fig. 8).

In any case, Fig. 11 a demonstrates that most contacts involving some binder stay in the soft branch and that the binder plays a dominant role for a large portion of the compaction. Recall, that the internal deformation of the graphite flakes also plays an important role on the total macroscopic stress (Fig. 8), but is not accounted in the contacts involving binder

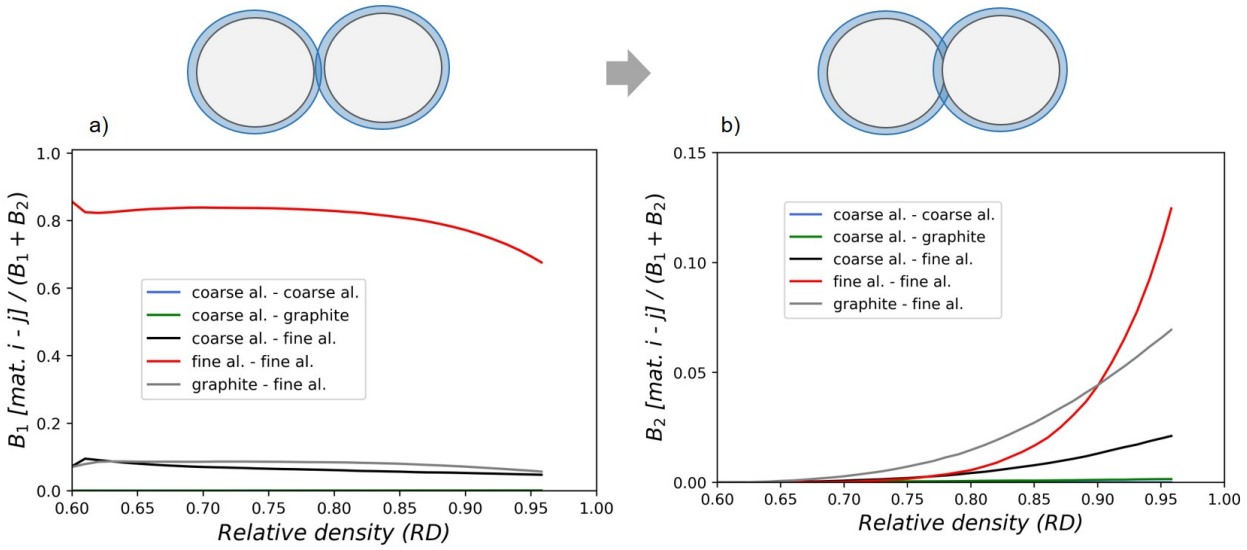

Figure 11: DEM close-die compaction simulation (target σ_z= 35 MPa, Mix R): fraction of contacts in a) the soft branch, and b) in the hard branch. B_1 and B_2 are the total number of contacts in the soft and hard branch, respectively.

shown in Fig. 11.

The fraction of contacts in branch 2 depends primarily on the volume fraction of binder (Fig. 12). A higher volume fraction of binder is associated, for a given stress or relative density, with a smaller fraction of contacts transitioning to branch 2 (hard phase). This is expected as the macroscopic deformation required to reach the critical indentation locally must be greater for a thicker binder coating.

We have also observed, that for a given relative density or a given stress, increasing the binder stiffness results in less contacts in branch 2. This is because reaching the critical indention becomes less frequent with stiffer binder. In any case, the binder stiffness has a significant impact on the macroscopic compaction stress (as indicated by Fig. 7), as a large majority of contacts remain in branch 1 dominated by the binder stiffness (Fig. 11).

7. Conclusions

In the present work, an original approach was developed based on a Representative Volume Element (RVE) to mimic the complex microstructure of model carbon-bonded alumina refractory composites. The compaction of the numerical microstructure was simulated using the discrete element method (DEM). Four compositions were studied by varying the volume

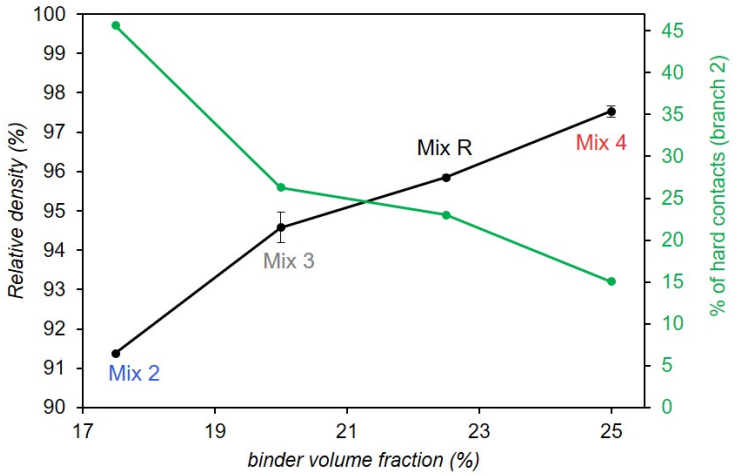

Figure 12: Evolution of the relative density (RD) of each composite, at 35 MPa, and the % of contacts in branch 2 (hard) at the end of the compaction.

fraction of each phase, within the typical range that is of interest for industrial applications. The composite in DEM was modeled by a mixture of single fine particles and bonded particle clusters (coarse alumina and graphite). For this purpose, a new contact models was developed to take into account the binder phase within the DEM framework. We have also shown the importance of carefully choosing the minimum number of discrete elements to ensure a good compromise between CPU time and model accuracy. When dealing with complex microstructures, this verification step is crucial as too small an RVE would lead to inaccurate results.

The main conclusion of this work is that for compositions of the order of 20 % volume fraction of binder, the binder stiffness dominates the mechanical response of the composite during compaction. Accordingly, varying the binder volume fraction will impact significantly the compaction behaviour. The DEM framework that we propose allows for a wealth of information to be obtained, leading to a more subtle picture of how these composites densify under compaction. In particular, it could lead to microstructure optimization to attain larger RDs for a given compacting stress.

Seeking simplicity, both in the implementation and the post-calculation analysis, we have chosen to represent coarse alumina particles as monosize spheres. The graphite was modelled by a rectangular geometry, also with monosize distribution. The real composite microstruc-

ture is clearly much more complex. It is characterized by irregular coarse alumina grains and graphite flakes with some dispersion in size and shape. We believe that the main results obtained here should remain valid for more realistic microstuctures. Ideally, the angular coarse alumina particles could be modelled by using X-ray tomography images. A number of individual real coarse alumina particles could be included in the simulation as proposed in [38].

Coarse and fine alumina hard particles were coated by an elastoplastic soft binder in DEM. This model aimed to represent in a simplified manner the presence of a soft coating on hard particles. The good qualitative and quantitative agreement with experimental compaction curves brings some confidence on the possibility of such a model to represent accurately a continuous matrix that cover most particles. The model includes some plasticity, once the contact has entered the hard-hard branch. It could be further improved by including some plasticity in the soft branch.

Acknowledgements The Association Nationale Recherche Technologie (ANRT), program CIFRE 2017/1583, is greatly acknowledged for its financial support.

References

[1] M. Lafer, D. Bouvard, P. Stutz, M. Pierronnet, G. Raisson, Influence of alumina inclusions on the densification of superalloy powder (Feb 1993).

[2] S. Roure, D. Bouvard, P. Dorémus, E. Pavier, Analysis of die compaction of tungsten carbide and cobalt powder mixtures, Powder Metallurgy 42 (2) (1999) 164–170.

[3] D. Bouvard, Densification behaviour of mixtures of hard and soft powders under pressure, Powder Technology 111 (3) (2000) 231–239.

[4] I. Aychn, B. J. Briscoe, K. Y. Sanhturk, The internal form of compacted ceramic components: a comparison of a finite element modelling with experiment, Powder Technology 89 (1996) 239–254.

[5] O. G. Abdullah, F. A. Rasin, T. A. Al-Dhahir, Finite element simulation of alumina ceramic powder compaction, International Journal of Pure and Applied Physics 5 (1) (2009) 15–31.

[6] S. Garner, J. Strong, A. Zavaliangos, The extrapolation of the Drucker-Prager/Cap material parameters to low and high relative densities, Powder Technology 283 (2015) 210–226.

[7] L. Perez-Gandarillas, A. Mazor, O. Lecoq, A. Michrafy, Compaction properties of dry granulated powders based on Drucker–Prager Cap model, Powder Technology 337 (2018) 43–50.

[8] J. Almanstötter, A modified Drucker-Prager Cap model for finite element simulation of doped tungsten powder compaction, International Journal of Refractory Metals and Hard Materials 50 (2015) 290–297.

[9] M. Zhou, S. Huang, J. Hu, Y. Lei, Y. Xiao, B. Li, S. Yan, F. Zou, A density-dependent modified Drucker-Prager Cap model for die compaction of Ag57.6-Cu22.4-Sn10-In10 mixed metal powders, Powder Technology 305 (2017) 183–196.

[10] V. Buljak, S. Baivier-romero, A. Kallel, Calibration of Drucker – Prager Cap Constitutive Model for Ceramic Powder Compaction through Inverse Analysis, Materials 14 (2021) 1–19.

[11] P. A. Cundall, O. D. Strack, A discrete numerical model for granular assemblies, Geotechnique 29 (1979) 331–336.

[12] C. L. Martin, D. Bouvard, S. Shima, Study of particle rearrangement during powder compaction by the Discrete Element Method, Journal of the Mechanics and Physics of Solids 51 (4) (2003) 667–693.

[13] O. Skrinjar, P. L. Larsson, Cold compaction of composite powders with size ratio, Acta Materialia 52 (7) (2004) 1871–1884.

[14] R. S. U. Ransing, D. T. Gethin, A. R. Khoei, P. Mosbah, R. W. Lewis, Powder compaction modelling via the discrete and finite element method, Materials Design 21 (2000) 263–269.

[15] R. S. Ransing, R. W. Lewis, D. T. Gethin, Using a deformable discrete-element technique to model the compaction behaviour of mixed ductile and brittle particulate systems, Philosophical Transactions of the Royal Society A: Mathematical, Physical and Engineering Sciences 362 (1822) (2004) 1867–1884.

[16] F. Huang, X. An, Y. Zhang, A. B. Yu, Multi-particle FEM simulation of 2D compaction on binary Al/SiC composite powders, Powder Technology 314 (2017) 39–48.

[17] K. Peng, H. Pan, Z. Zheng, J. Yu, Compaction behavior and densification mechanisms of Cu-W composite powders, Powder Technology 382 (2021) 478–490.

[18] C. L. Martin, D. Bouvard, Isostatic compaction of bimodal powder mixtures and composites, International Journal of Mechanical Sciences 46 (6) (2004) 907–927.

[19] K. Wu, S. Rémond, N. E. Abriak, P. Pizette, F. Becquart, S. Liu, Study of the shear behavior of binary granular materials by DEM simulations and experimental triaxial tests, Advanced Powder Technology 28 (9) (2017) 2198–2210.

[20] C. Ramírez-Aragón, J. Ordieres-Meré, F. Alba-Elías, A. González-Marcos, Comparison of Cohesive models in EDEM and LIGGGHTS for simulating powder compaction, Materials 11 (11) (2018) 1–17.

[21] C. Ramírez-Aragón, J. Ordieres-Meré, F. Alba-Elías, A. González-Marcos, Numerical modeling for simulation of compaction of refractory materials for secondary steelmaking, Materials 13 (1) (2020) 1–21.

[22] L. Salvo, P. Cloetens, E. Maire, S. Zabler, J. J. Blandin, J. Y. Buffière, W. Ludwig, E. Boller, D. Bellet, C. Josserond, X-ray micro-tomography an attractive characterisation technique in materials science, Nuclear Instruments and Methods in Physics Research, Section B: Beam Interactions with Materials and Atoms 200 (2003) 273–286.

[23] K. Szarf, G. Combe, P. Villard, Polygons vs. clumps of discs: A numerical study of the influence of grain shape on the mechanical behaviour of granular materials, Powder Technology 208 (2) (2011) 279 – 288. arXiv:1208.0565.
URL http://www.sciencedirect.com/science/article/pii/S0032591010004092

[24] I. Ostanin, R. Ballarini, D. Potyondy, T. Dumitrică, A distinct element method for large scale simulations of carbon nanotube assemblies, Journal of the Mechanics and Physics of Solids 61 (3) (2013) 762–782. doi:10.1016/j.jmps.2012.10.016.

[25] B. V. Derjaguin, V. M. Muller, Y. P. Toporov, Effect of contact deformation on the adhesion of elastic solids, Journal of Colloid and Interface Science 53 (2) (1975) 314–326.

[26] K. Johnson, Contact Mechanics, Cambridge University Press, 1987.

[27] G. Jefferson, G. K. Haritos, R. M. McMeeking, The elastic response of a cohesive aggregate - A discrete element model with coupled particle interaction, Journal of the Mechanics and Physics of Solids 50 (12) (2002) 2539–2575.

[28] D. Jauffres, C. L. Martin, A. Lichtner, R. K. Bordia, D. Jauffrès, C. L. Martin, A. Lichtner, R. K. Bordia, Simulation of the toughness of partially sintered ceramics with realistic microstructures, Acta Mater. 60 (2012) 4685–4694.

[29] C. L. Martin, D. Bouvard, G. Delette, Discrete element simulations of the compaction of aggregated ceramic powders, Journal of the American Ceramic Society 89 (11) (2006) 3379–3387.

[30] P. Pizette, C. L. Martin, G. Delette, F. Sans, T. Geneves, Green strength of binder-free ceramics, Journal of the European Ceramic Society 33 (5) (2013) 975–984.

[31] D. O. Potyondy, P. A. Cundall, A bonded-particle model for rock, International Journal of Rock Mechanics and Mining Sciences 41 (8 SPEC.ISS.) (2004) 1329–1364.

[32] J. Weber, Recherches concernant les contraintes intergranulaires dans les milieux pulvérulents, Bulletin de liaison des Ponts et Chaussées, (1966) 1–20.

[33] J. Christoffersen, A Micromechanical Description of Granular Material Behavior, Journal of Applied Mechanics 48 (1981) 67.

[34] C. L. Martin, R. K. Bordia, Influence of adhesion and friction on the geometry of packings of spherical particles, Physical Review E - Statistical, Nonlinear, and Soft Matter Physics 77 (3) (2008) 1–8.

[35] R. Kumar, S. Rommel, D. Jauffrès, P. Lhuissier, C. L. Martin, Effect of packing characteristics on the discrete element simulation of elasticity and buckling, International Journal of Mechanical Sciences 110 (2016) 14–21.

[36] I. Agnolin, J.-N. Roux, Internal states of model isotropic granular packings. I. Assembling process, geometry, and contact networks, Phys. Rev. E 76 (2007) 61302.

[37] K. Radi, D. Jauffrès, S. Deville, C. L. Martin, Elasticity and fracture of brick and mortar materials using discrete element simulations, Journal of the Mechanics and Physics of Solids 126 (2019) 101–116.

[38] K. Radi, H. Saad, D. Jauffres, S. Meille, T. Douillard, S. Deville, C. L. Martin, Effect of microstructure heterogeneity on the damage resistance of nacre-like alumina: Insights from image-based discrete simulations, Scripta Materialia 191 (2021) 210–214.